Geophysical Journal International

Geophys. J. Int. (2016) **207,** 1030–1048
Advance Access publication 2016 August 22
GJI Seismology

doi: 10.1093/gji/ggw313

Variation in high-frequency wave radiation from small repeating earthquakes as revealed by cross-spectral analysis

Norishige Hatakeyama,[1,*] Naoki Uchida,[1] Toru Matsuzawa,[1] Tomomi Okada,[1] Junichi Nakajima,[2] Takeshi Matsushima,[3] Toshio Kono,[1] Satoshi Hirahara[1] and Takashi Nakayama[1]

[1]*Research Center for Prediction of Earthquakes and Volcanic Eruptions, Graduate School of Science, Tohoku University, Sendai* 980-8578, *Japan. E-mail: nori.hatake@outlook.com*
[2]*Department of Earth and Planetary Sciences, Graduate School of Science and Engineering, Tokyo Institute of Technology, Tokyo* 152-8551, *Japan*
[3]*Institute of Seismology and Volcanology, Faculty of Science, Kyushu University Shimabara city, Nagasaki* 855-0843, *Japan*

Accepted 2016 August 17. Received 2016 June 21; in original form 2015 December 13

SUMMARY

We examined the variation in the high-frequency wave radiation for three repeating earthquake sequences ($M = 3.1$–4.1) in the northeastern Japan subduction zone by waveform analyses. Earthquakes in each repeating sequence are located at almost the same place and show low-angle thrust type focal mechanisms, indicating that they represent repeated ruptures of a seismic patch on the plate boundary. We calculated cross-spectra of the waveforms and obtained the phases and coherences for pairs of events in the respective repeating sequences in order to investigate the waveform differences. We used waveform data sampled at 1 kHz that were obtained from temporary seismic observations we conducted immediately after the 2011 Tohoku earthquake near the source area. For two repeating sequences, we found that the interevent delay times for the two waveforms in a frequency band higher than the corner frequencies are different from those in a lower frequency band for particular event pairs. The phases and coherences show that there are coherent high-frequency waves for almost all the repeaters regardless of the high-frequency delays. These results indicate that high-frequency waves are always radiated from the same vicinity (subpatch) for these events but the time intervals between the ruptures of the subpatch and the centroid times can vary. We classified events in the sequence into two subgroups according to the high-frequency band interevent delays relative to the low-frequency band. For one sequence, we found that all the events that occurred just after (within 11 days) larger nearby earthquakes belong to one subgroup while other events belong to the other subgroup. This suggests that the high-frequency wave differences were caused by stress perturbations due to the nearby earthquakes. In summary, our observations suggest that high-frequency waves from the repeating sequence are radiated not from everywhere but from a long-duration subpatch within the seismic slip area. The variation in high-frequency radiation can be explained by rupture pattern differences that depend on the stress conditions in and around the seismic patches.

Key words: Fourier analysis; Seismic cycle; Earthquake dynamics; Earthquake source observations; Earthquake interaction, forecasting, and prediction; Dynamics and mechanics of faulting.

1 INTRODUCTION

Earthquake rupture processes usually differ from event to event even if they rupture almost the same areas. Many researchers have studied the rupture processes for large recurrent earthquakes that occurred along the plate boundary, including the northeastern Japan subduction zone. Nagai *et al*. (2001) estimated the rupture processes for the 1968 Tokachi-oki earthquake (M7.9) and the 1994 Sanriku-haruka-oki earthquake (M7.6) from the waveform modelling. They showed that the main rupture area of the 1994 event corresponds to one of the asperities (large slip areas) that were ruptured by the 1968 event. The rupture area for the Miyagi-oki earthquake sequence is also characterized by complicated rupture patterns. Umino *et al*.

[*] Now at: Mitsubishi Research Institute, Inc., Tokyo 100-8141, Japan.

(2006) suggested the 1933 (*M*7.1), 1936 (*M*7.4) and 1937 (*M*7.1) Miyagi-oki earthquakes might have ruptured parts of the source area for the 1978 event (*M*7.4) based on the relocated aftershock distributions. Waveform modelling studies indicate that part of the slip area for the 1978 event was re-ruptured by the 2005 *M*7.2 event (Okada *et al*. 2005; Wu *et al*. 2008). These researches suggest that there are some unit areas (seismic patches or asperities) that can cause recurrent earthquakes, but the combinations of patches that slip seismically in respective ruptures are not always the same.

Rupture processes of a single seismic patch can also vary somewhat. Yamanaka & Kikuchi (2004) estimated the seismic slip distributions for large interplate earthquakes that occurred in the northeastern Japan subduction zone in the twentieth century. They showed that the rupture areas for the 1994 Sanriku-haruka-oki earthquake and the 1931 earthquake (*M*7.6) are associated with the same asperity but their rupture initiation points (i.e. hypocentres) are different. The same situation applies to the 1960 (*M*7.2) and 1989 (*M*7.1) earthquakes off Iwate. For medium-sized earthquakes, Shimamura *et al*. (2011) performed the waveform modelling to estimate the rupture processes for the $M \sim 4.8$ Kamaishi-oki earthquake series, which have occurred repeatedly on the plate boundary in the northeastern Japan subduction zone. They found that both the 2001 and 2008 events ruptured the same asperity but their rupture processes are slightly different, which explains the waveform differences in the high-frequency components. For the repeaters along the San Andreas Fault in Parkfield, Kim *et al*. (2016) investigated rupture processes for an *M*2.1 repeating earthquake sequence and observed notable peak slip reduction just after the 2004 *M*6.0 Parkfield earthquake.

Additionally, locations and sizes of strong motion generation areas (SMGAs), which are the origins of strong ground motions that contain large amounts of high-frequency energy, were examined for repeated ruptures associated with some large interplate earthquakes. Suzuki & Iwata (2007) estimated SMGAs for the 2005 Miyagi-oki earthquake and compared them to those for the 1978 Miyagi-oki earthquake estimated by Kamae *et al*. (2002). They showed that the SMGAs for the two events do not overlap. Takiguchi *et al*. (2011) estimated SMGAs for the 1982 (*M*7.0) and 2008 (*M*7.0) Ibaraki-oki earthquakes, which showed similar aftershock distributions so that these earthquakes are thought to have ruptured almost the same area. They pointed out the possibility that the SMGAs for the 1982 and 2008 events overlap.

These previous studies indicate that the rupture processes for recurrent earthquakes show wide ranges of varieties especially with regard to high-frequency radiation. It is important to reveal the source of variation in rupture processes, both to understand the source physics of earthquakes and for seismic hazard estimation. For these purposes, investigating the rupture processes in detail for many recurrences and examining their variability and regularity are necessary.

In this study, we focus on variations in the rupture processes for small repeating earthquakes ($M \sim 3$–4), which can be explained by repeated ruptures of a small seismic patch on a fault plane (e.g. Matsuzawa *et al*. 2002; Igarashi *et al*. 2003). Investigating such simple recurrent earthquake sequences is a good starting point for understanding the variation in ruptures for earthquakes that occur in the same place. Moreover, the recurrence intervals for small repeating earthquakes are shorter than those for larger recurrent earthquakes and we can obtain a large amount of data even in the short period for which recent high-quality data are available. Both small and large interplate earthquakes are caused by the ruptures on the plate boundary and the rupture processes are considered to be essentially the same even though the dimensions are different. Therefore, the investigation of small earthquakes can help us understand large earthquakes.

Generally, large earthquakes provide strong signals in wide frequency ranges to seismic networks and it is relatively easy to investigate their rupture processes by waveform analyses. In order to reveal the rupture processes for small earthquakes with higher corner frequencies, however, we have to carry out high rate observations and detailed analyses of the high-frequency components of the waveforms.

Throughout this study, we define 'repeating earthquakes' as events whose rupture areas mostly overlap. Such earthquakes are identified based on the waveform similarity (e.g. Uchida & Matsuzawa 2013) and the colocation of the slip areas are confirmed in this study. In that case, the waveforms for repeating earthquakes are expected to be similar in the frequency bands lower than their corner frequencies. We focus on the frequency bands higher than corner frequencies, which have the information about the rupture processes whose scales are smaller than their rupture areas. Thus we hereafter refer high- and low-frequency components relative to their corner frequencies.

We examine the differences among the high-frequency components of waveforms for events belonging to the same repeating earthquake sequences by cross-spectral analyses. We show that high-frequency waves vary for the analysed repeating earthquakes but they are not radiated at random. We propose a provisional model that can explain the variation in the high-frequency radiation.

2 HIGH RATE OBSERVATIONS

We performed 1 kHz sampling rate seismic observations at three permanent borehole stations (HS5, MY3 and SN3; 300–500 m in depth) operated by Tohoku University along the Sanriku Coast of northeastern Japan immediately after the 2011 *M*9.0 Tohoku earthquake (Tohoku EQ; Fig. 1). The seismometers at stations HS5 and SN3 are located in bedrocks of granodiorite while MY3 is located in granite. This is one of the first high sampling rate recordings targeted at subduction zone interplate earthquakes. At these stations, we deployed 1 kHz sampling rate data loggers (EDR-X7000, manufactured by Kinkei System Corporation) for the period from late April to mid-November 2011. Continuous waveform data were stored in compact flash cards and retrieved once a month. The seismometers at these stations are the 1 Hz velocity type. Note that we can examine the features of waveforms only up to ∼30 Hz using conventional 100 Hz sampled data telemetered from the stations, but the 1 kHz sampled data enable us to examine frequency bands higher than 30 Hz.

3 TARGETED REPEATING EARTHQUAKE SEQUENCES

We analysed three repeating earthquake sequences named groups A, B and C off Iwate prefecture in northeastern Japan to examine differences among the high-frequency components of their waveforms. Their locations are relatively close to the coast where the high rate observations were conducted: epicentral distances to the stations are ∼37–100 km (Fig. 1). These sequences were chosen from an updated repeating earthquake catalogue by Uchida & Matsuzawa (2013), in which repeating earthquakes were selected based on waveform similarity in 1–8 Hz or lower frequency bands. Almost all of the repeating earthquakes in the catalogue occurred on the boundary between the subducting Pacific plate and the overriding

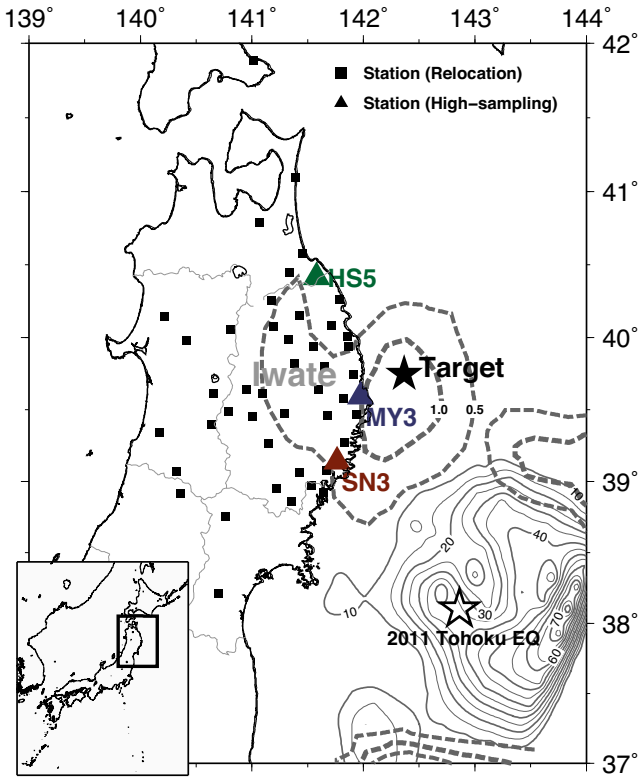

Figure 1. Map showing the location of repeating earthquake sequences (solid star) off Iwate-prefecture, northeastern Japan, analysed in this paper. The solid triangles and squares, respectively, show seismic stations for the data sampled at 1 kHz that are used in the high-frequency waveform analyses (HS5, MY3 and SN3) and stations used for earthquake relocation. The open star and solid grey contour lines indicate the hypocentre and coseismic slip distribution (Iinuma *et al*. 2012) for the 2011 *M*9.0 Tohoku EQ, respectively. The broken grey contour lines indicate the 1-yr afterslip distribution for the Tohoku EQ (Sun & Wang 2015). The rectangle in the lower left map denotes the area shown in the main map.

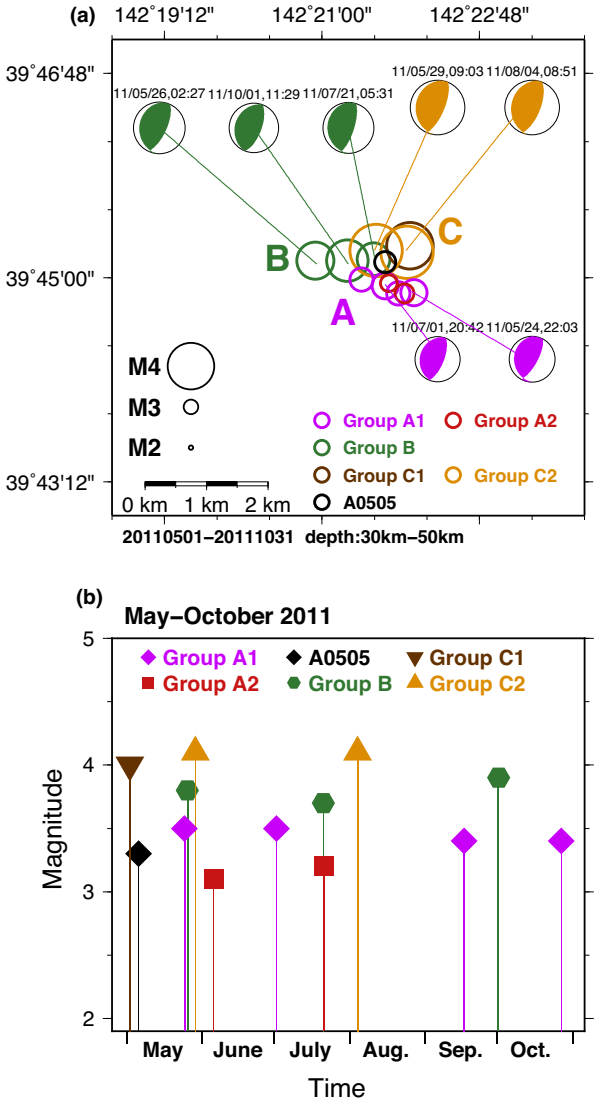

Figure 2. (a) Earthquake locations in the study region for the period from May to October 2011. Earthquakes located at depths from 30 to 50 km are shown here. The hypocentres are from the unified catalogue of the Japan Meteorological Agency. The pink, red, green, brown and orange circles show events in groups or subgroups A1, A2, B, C1 and C2, respectively, and the black circle shows an *M*3.3 event on 2011 May 5 (A0505), which is not included in the original repeating earthquake catalogue but is located at almost the same place as group A events as shown in Fig. 3. Note that we divided group A into A1 and A2, and group C into C1 and C2 based on the high-frequency delay patterns as shown in Section 5. The size of each circle represents the expected source area, assuming a stress drop of 10 MPa. Focal mechanisms are from the F-net focal mechanism catalogue by the National Research Institute for Earth Science and Disaster Resilience, Japan. (b) Magnitude-time diagram in the region shown in Fig. 2(a) for the period from May to October 2011 (study period). The pink diamonds (A1), red squares (A2), green hexagons (B), inverted brown triangle (C1) and orange triangles (C2) denote groups or subgroups. The black diamond denotes the *M*3.3 event on 2011 May 5 (A0505).

continental plate. Fig. 2(a) shows a close-up view of the epicentre distribution of the target events in the place indicated by the solid star in Fig. 1. The selected sequences are located very close to each other and the focal depths are ∼40 km, which corresponds to the depth to the plate boundary in this region. We selected these events because there have been no larger or comparable-sized earthquakes within 5 km from these sequences since at least 2000. This means that interactions with other earthquakes should be relatively weak for these sequences.

We examined the events in the period from May to October 2011, during which we performed the 1 kHz sampling rate seismic observations. Note that even though the observation period is only a half year, we recorded many events for each repeating sequence because of frequent repeater occurrences as a result of the large afterslip associated with the Tohoku EQ (e.g. Uchida & Matsuzawa 2013; Sun & Wang 2015). Such increased frequency of repeaters was often found after large interplate earthquakes (e.g. Uchida *et al*. 2003, 2004; Chen *et al*. 2010). In the repeating earthquake catalogue, groups A, B and C include six, three and three events, respectively, during this period. Fig. 2(b) shows a magnitude–time diagram for the events shown in Fig. 2(a). The magnitudes reported in the unified earthquake catalogue by the Japan Meteorological Agency (JMA) are *M*3.1–3.5 for group A, *M*3.7–3.9 for group B and *M*4.0–4.1 for group C (Fig. 2b). The focal mechanisms reported in the F-net catalogue by the National Research Institute for Earth Science and Disaster Resilience (NIED), Japan are also shown in Fig. 2(a). They all show low-angle thrust type, which indicates that they occurred on the plate boundary.

The size of each circle in Fig. 2(a) indicates the expected source radius r for each event estimated from the magnitude (M) assuming

Table 1. Earthquakes analysed in this study. The origin times and magnitudes are from the JMA unified hypocentre catalogue.

	Year	Mon.	Day	Hour	Min.	Sec.	Mag.
A0505	2011	5	5	9	38	6	M3.3
A0524	2011	5	24	22	3	18	M3.5
A0605	2011	6	5	20	50	36	M3.1
A0701	2011	7	1	20	42	19	M3.5
A0721	2011	7	21	9	41	56	M3.2
A0917	2011	9	17	5	45	44	M3.4
A1027	2011	10	27	8	36	32	M3.4
B0526	2011	5	26	2	27	35	M3.8
B0721	2011	7	21	5	31	1	M3.7
B1001	2011	10	1	11	29	49	M3.9
C0502	2011	5	2	9	38	6	M4.0
C0529	2011	5	29	9	3	7	M4.1
C0804	2011	8	4	8	51	52	M4.1

the stress drop ($\Delta\sigma$) of 10 MPa using the formulas of Hanks & Kanamori (1979):

$$\log(M_0) = 1.5M + 9.1, \tag{1}$$

and Eshelby (1957):

$$\Delta\sigma = (7/16)\left(M_0/r^3\right), \tag{2}$$

where M_0 is the seismic moment in Nm. The assumed stress drop is a typical value for interplate earthquakes in this region (Uchida *et al*. 2012; Uchide *et al*. 2014). We estimated the source sizes assuming a circular crack model, constant stress drops and M_w = Mjma for simplicity as we do not discuss the rupture areas for respective events in detail.

Other than the group A, B and C events in the repeating earthquake catalogue, an *M*3.3 event on 2011 May 5 (A0505) is located at almost the same location as these groups in the JMA unified catalogue. We regard this event as an earthquake belonging to group A based on the hypocentre relocation that we describe in Section 4.

The occurrence times and magnitudes for these events are listed in Table 1. Hereafter, we name each event using the nomenclature 'XMMDD', where X indicates the group name (A–C), and MMDD represents the occurrence date (month and day) of the event (Table 1). For example, A0524, B0721 and C0804 represent the group A event on 2011 May 24, the group B event on July 21, and the group C event on August 4, respectively.

4 HYPOCENTRE RELOCATION FOR TARGET REPEATERS

Before carrying out the waveform analyses using the high sampling rate data, we performed hypocentre relocations for the 13 events in the three repeating earthquake sequences during the observation period in order to confirm that groups A–C, respectively constitute spatially separated repeating clusters. We used the waveform-based double-difference method (Waldhauser & Ellsworth 2000; Uchida *et al*. 2012) and 100 Hz sampled waveform data for the relocation. Arrival time differences were measured using the cross-spectral method (Poupinet *et al*. 1984) for both *P* and *S* waves. We set a 3.55 s time window starting from 0.7 s before the onset of each phase. We then estimated arrival time differences between events from the phases of cross-spectra with coherences greater than 0.75 in a frequency band of 1–10 Hz. The seismic stations used for the arrival time measurements are shown as solid squares in Fig. 1. The stations belong to JMA, NIED, Hokkaido University, Hirosaki University and Tohoku University. Most of the seismometers are the 1 Hz velocity type. For the 13 events, we obtained 3041 and 2186 differential arrival time observations for P and S phases, respectively. Note that the event locations estimated from the cross-spectra are not the rupture initiation points but correspond to the centroids of the moment release distributions (e.g. Fremont & Malone 1987).

The centroid locations after the relocation are shown in Fig. 3. We found that the events in each group were relocated at almost the same location, indicating that groups A–C respectively constitute separate sequences as expected from the waveform-similarity analysis of Uchida & Matsuzawa (2013). The location uncertainties were estimated to be ∼5 m in the north–south direction, ∼10 m in the east–west direction, and ∼15 m in depth. Event A0505 was relocated to a position nearly identical to the group A events. We thus classified the event A0505 into group A in the waveform analyses described later, although it was not identified as such by Uchida & Matsuzawa (2013). Intergroup distances among the estimated centroid locations for groups A–C are within 1 km, which is comparable to the expected source dimensions for ∼*M*3–4 earthquakes. This suggests that these repeating earthquakes may have strongly interacted with each other.

Fig. 4 shows examples of vertical (UD) component waveforms for the target events observed at station MY3 (the deep-blue triangle in Fig. 1). In each group, highly similar waveforms were obtained for each component and each station, though their magnitudes fluctuated a little. Waveform examples for stations HS5 and SN3 are shown in Figs S1 and S2, respectively.

The signal-to-noise ratios (S/N) for all the waveforms are >5 in a frequency range up to at least ∼50 Hz, where S/N is defined as the spectral amplitude ratio of the *P* wave to the noise before the *P* wave arrival (Figs S3–S5). Note that electrical noises are large at 50 Hz, corresponding to the commercial power frequency in eastern Japan.

5 CROSS-SPECTRAL ANALYSIS OF WAVEFORMS FOR THE REPEATING EARTHQUAKES

5.1 Method

To investigate waveform differences in the high-frequency components for two events belonging to the same repeating earthquake sequence, we calculated cross-spectra to obtain the phases and coherences. Since the two events occurred in almost the same location, we can consider the difference in the waveform to originate mainly from the difference in the rupture process. We carried out the cross-spectral analyses described below for all the pairs in each group.

In general, the cross-spectrum $c_{xy}(f)$ of two time domain waveforms $x(t)$ and $y(t)$ is written as:

$$c_{xy}(f) = \langle X^*(f)\, Y(f)\rangle, \tag{3}$$

where $X(f)$ and $Y(f)$ are the Fourier spectra for x and y, respectively; X^* indicates the complex conjugate of X; and $\langle\rangle$ indicates the expected value.

In this study, we estimated the expected value of the product of X^* and Y at a frequency f_i using weighted smoothing in the frequency domain:

$$\langle X^*(f_i)\, Y(f_i)\rangle = \frac{1}{n_f^2}\Big[n_f X^*(f_i)\, Y(f_i) + \sum_{n=1}^{n_f-1}\left(n_f - n\right) \times \left\{X^*(f_{i-n})\, Y(f_{i-n}) + X^*(f_{i+n})\, Y(f_{i+n})\right\}\Big], \tag{4}$$

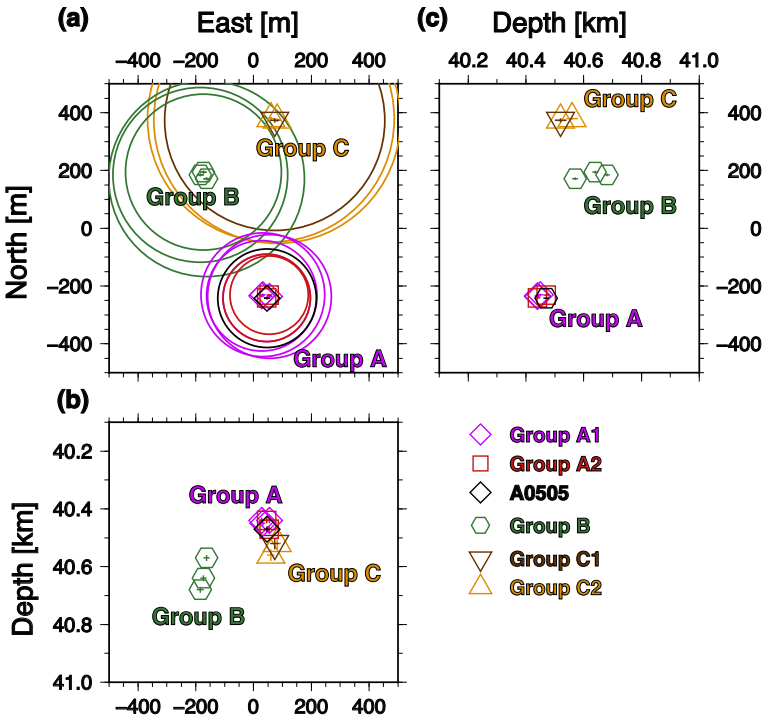

Figure 3. Relocated centroid distribution for earthquakes in the repeating sequences from May to October 2011. (a) Map view. (b) East–west cross section. (c) North–south cross section. The pink diamonds (A1), red squares (A2), green hexagons (B), inverted brown triangles (C1) and orange triangles (C2) denote groups or subgroups, and the black diamonds denote the *M*3.3 event on 2011 May 5 (A0505). The small bars denote the centroid location errors for the respective directions. In Fig. 3(a), the size of each circle represents the expected source area assuming a stress drop of 10 MPa. Note that the subgroups A1/A2 and C1/C2 were defined based on their high-frequency phase delay patterns.

where the constant n_f determines the strength of smoothing in the frequency domain.

The phase $\phi(f_i)$ and coherence $coh(f_i)$ for seismograms $x(t)$ and $y(t)$ are defined as:

$$\phi(f_i) = \arctan\left[\mathrm{Im}\left(c_{xy}(f_i)\right)/\mathrm{Re}\left(c_{xy}(f_i)\right)\right], \tag{5}$$

$$coh(f_i) = \left|c_{xy}(f_i)\right| / \sqrt{P_x(f_i)\,P_y(f_i)}. \tag{6}$$

$P_x(f_i)$ and $P_y(f_i)$ represents power spectrum for $x(t)$ and $y(t)$, respectively, which are calculated as:

$$P_x(f_i) = \langle X^*(f_i)\,X(f_i)\rangle, \tag{7a}$$

$$P_y(f_i) = \langle Y^*(f_i)\,Y(f_i)\rangle. \tag{7b}$$

The coherence represents the degree of waveform similarity in a narrow band around a frequency f_i and takes values from 0 to 1: coherence becomes 1 when the two waveforms are identical in the frequency band. The phase ($\Delta t_{\mathrm{phase}}$) and group ($\Delta t_{\mathrm{group}}$) delay times between the two waveforms (interevent delays) are, respectively, calculated as:

$$\Delta t_{\mathrm{phase}} = \phi(f)/2\pi f, \tag{8}$$

$$\Delta t_{\mathrm{group}} = (1/2\pi)\,\partial\phi(f)/\partial f. \tag{9}$$

In calculating the waveform cross-spectra, we aligned two waveforms so that the calculated phases in their low-frequency bands (2–8 Hz for group A, 1.5–6 Hz for group B and 1–4 Hz for group C) were close to zero (i.e. the interevent low-frequency delay became zero). The upper limits of the frequency bands were set to be almost the same as the corner frequencies expected for the events in the sequences and the lower limits are two octaves lower than the upper limits.

We performed the cross-spectral analyses using three time windows: a 4.096 s window starting 0.5 s before the *P* wave onset (P-window; left shaded region in Fig. 4), a 4.096 s window starting 0.5 s before the *S* wave onset (S-window; right shaded region in Fig. 4), and a 32.768 s window from 3.5 s before the *P* wave onset (F-window; full length in Fig. 4). The Fourier spectra $X(f_i)$ and $Y(f_i)$ were calculated after applying cosine tapers to the first 10 per cent and last 10 per cent of the windows. For group A, we adopted the n_f values in eq. (4) of 8 for the P- and S-windows and 64 for the F-window. These values correspond to a frequency window of $\pm\sim$2.0 Hz for the weighted smoothing. For groups B and C, the n_f values are 6 for the P- and S-windows and 48 for the F-window, which correspond to $\pm$1.5 Hz smoothing windows. We set larger values of n_f for group A for which we focused on higher frequency band than the others because amplitudes of the Fourier spectrum become smaller and phases of cross-spectra are likely to be unstable as the frequencies become high. We calculated the phases and coherences for all possible pairs in each sequence and for the three stations and three components of the seismograms.

5.2 Results

5.2.1 Group A

In Fig. 5, we show the phases of cross-spectra calculated using the S-window for all event pairs in group A. The shaded regions in Fig. 5 indicate the ranges of expected corner frequencies f_c estimated from

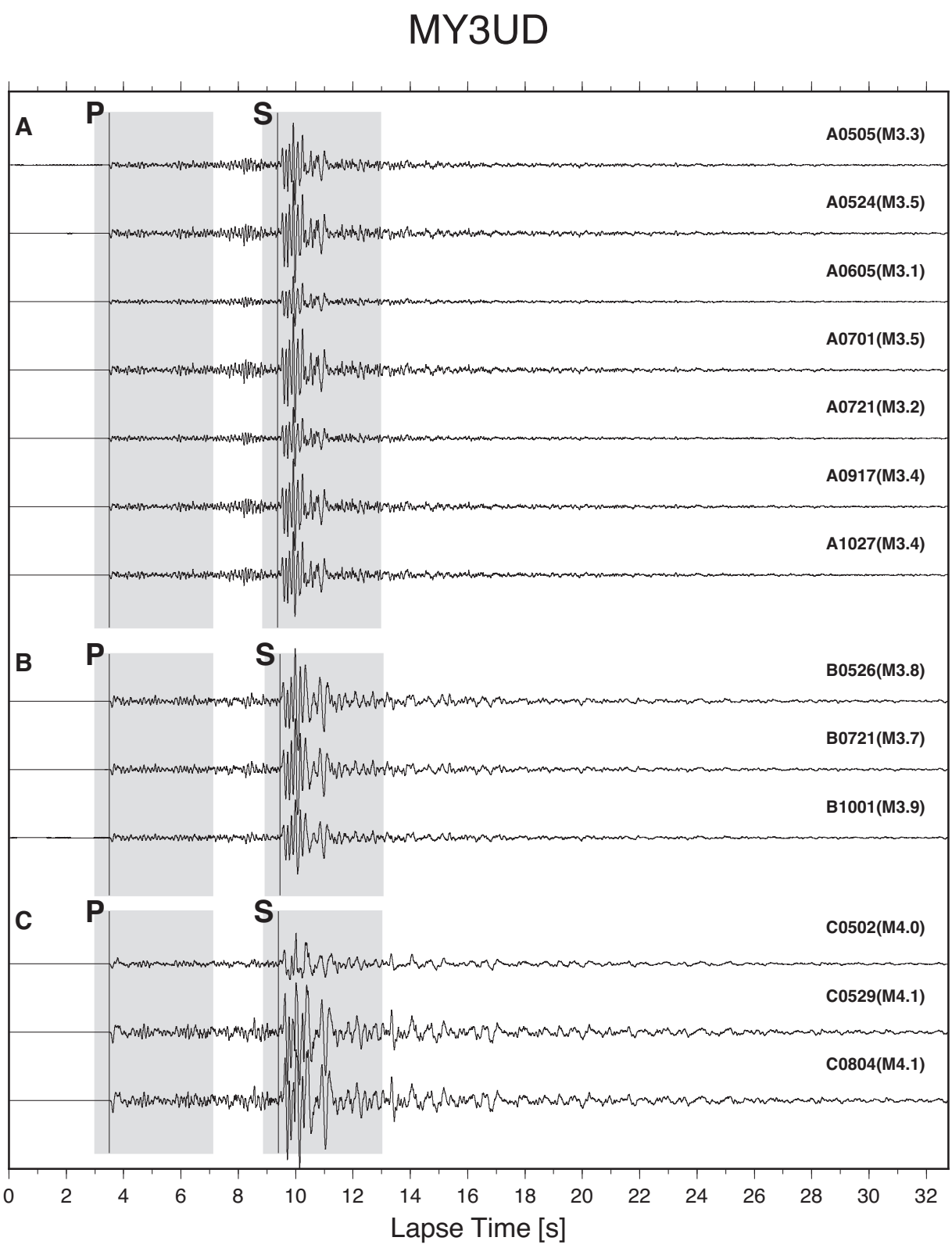

Figure 4. Examples of raw waveforms for events in groups A–C for the vertical (UD) component at station MY3. The traces for groups A, B and C are, respectively, scaled to the maximum amplitudes of events A0524, B0721 and C0529. All traces are plotted so that the onsets of their *P* waves are aligned. The vertical lines indicate the arrival times of *P* and *S* waves. The shaded regions indicate the 4.096 s time windows used in the analyses for *P* and *S* waves.

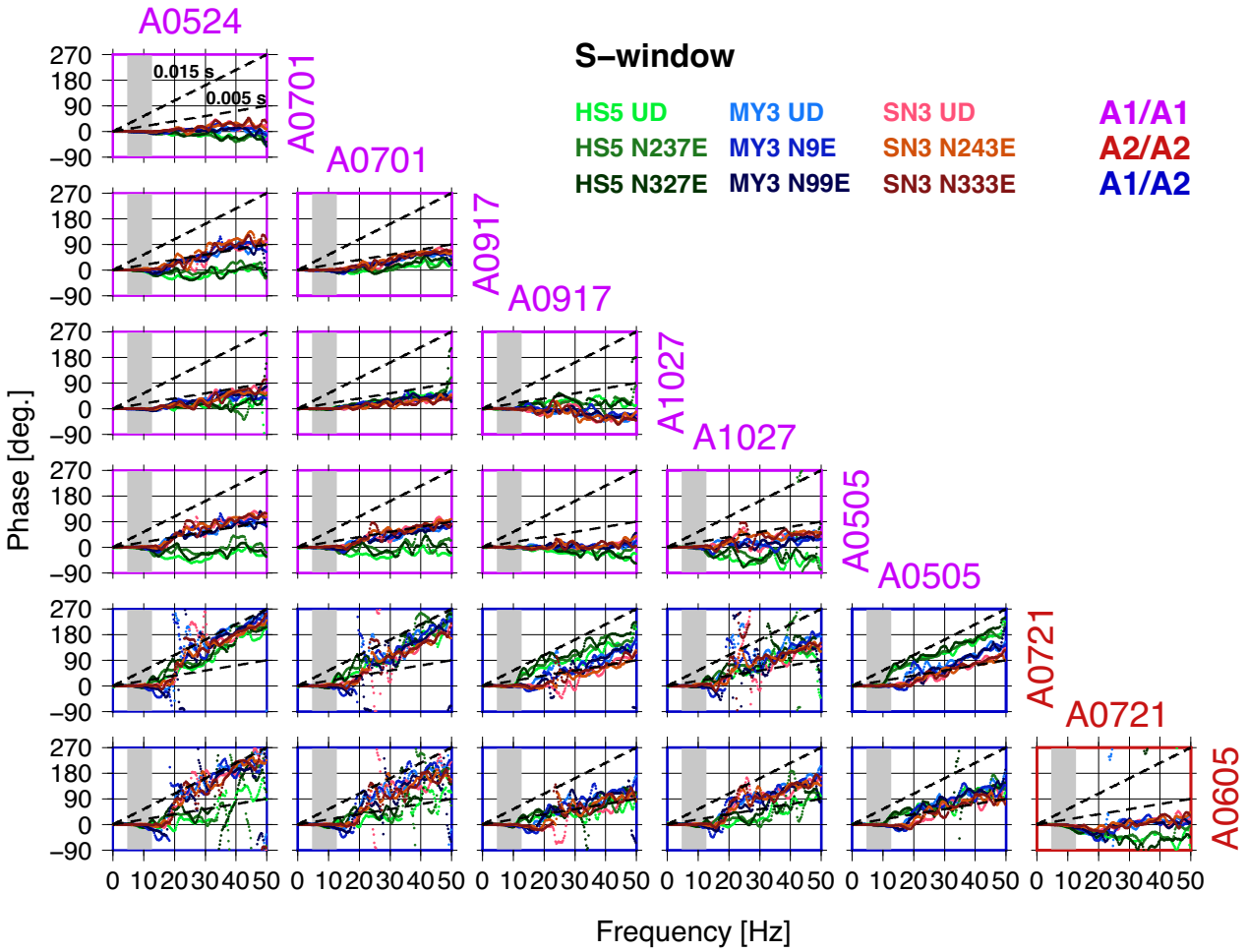

Figure 5. Phases of S-window cross-spectra for all event pairs in group A. The colours of the traces indicate the station-component sets as shown in the upper right. The colours of the frames show the combinations of the pairs (pink: A1/A1, red: A2/A2 and blue: A1/A2). The shaded regions indicate the range of expected *S*-wave corner frequencies for M3.1–3.5 events using the model of Sato & Hirasawa (1973) and assuming stress drops of 5–20 MPa. The broken black lines represent the inclination angles corresponding to 0.005 and 0.015 s time delays. For the A1/A2 pairs, positive slopes mean that the delay time in the high-frequency band relative to low-frequency band for A2 is larger than that for A1. Note that we calculated cross-spectra after aligning the two waveforms so that the calculated phases in the 2–8 Hz range became zero.

the range of source radii (r) using the model of Sato & Hirasawa (1973):

$$r = Cv/2\pi f_c, \tag{10}$$

where v is the phase velocity (7.8 and 4.4 km s^{-1} for P and S waves, respectively) and C is a constant (1.5 and 1.9 for P and S waves, respectively). The range of source radii is estimated from the range of earthquake magnitudes using eqs (1) and (2) with assumed stress drops of 5–20 MPa. Since we just wanted to know the corner frequency as an approximate boundary between low- and high-frequency components, we estimated expected corner frequencies using such simple assumptions in this study.

For pairs in blue frames in Fig. 5, the phases in the frequency band higher than the corner frequencies show significantly different inclination angles from those in the lower-frequency band. This indicates that interevent delays in the high-frequency band (∼20–50 Hz) are different from those in the low-frequency band (∼2–8 Hz) for these pairs. For given pairs of events, the phases calculated for all the stations and components, represented by different colours in Fig. 5, show similar delay patterns.

We found that the high-frequency phase gradients, corresponding to group delays (eq. 9), are similar to the gradients for straight lines passing through the origin and each phase value, corresponding to phase delays (eq. 8). It means that the interevent delays can be considered both to be the group delays and to be the phase delays. We can see that the delays for A1/A2 pairs are ∼0.005–0.015 s from the inclination angles of the frequency-phase diagrams (see broken lines in Fig. 5). In order to confirm the differences in the interevent delay between the high- and low-frequency bands (hereafter DDHLs), we show examples of filtered waveforms for events in group A around their *S* wave arrival times in Fig. 6. The traces in (a), (b) and (c), respectively show raw waveforms, 2–8 Hz bandpass filtered waveforms, and 30–45 Hz bandpass filtered waveforms superimposed so that the time lags among the 2–8 Hz filtered waveforms are zero. The traces in (d) are the same as the traces in (c) except they are superimposed so that the time lags among the 30–45 Hz filtered waveforms are zero. Comparing the traces in (c) and (d), we can see that there are differences between time lags in the high- and low-frequency components for some event pairs even though they are expected to share the same source areas. This indicates the DDHL originates from the interevent difference

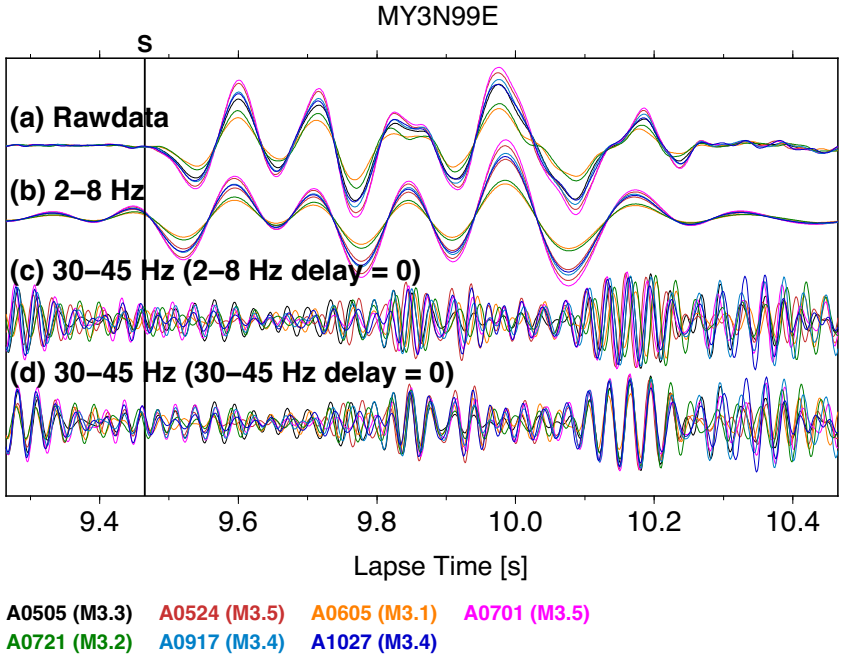

Figure 6. Examples of velocity seismograms from group A at station MY3. N99E component waveforms around the *S*-wave arrival times are shown. The vertical line indicates the *S* wave arrival times. (a) Raw data superimposed so that the delays for the 2–8 Hz range become zero. (b) Same as (a) but 2–8 Hz bandpass filtered. (c) Same as (a) but 30–45 Hz bandpass filtered. (d) Same as (c) but superimposed so that the delays for the 30–45 Hz range become zero. Seismograms from different events are drawn in different colours as shown at the bottom.

in the timing of high-frequency wave arrival relative to that of low-frequency wave.

From the cross-spectra phase results, we regrouped group A into subgroups A1 and A2 by the delay patterns as shown in Fig. 5: events A0505, A0524, A0701, A0917 and A1027 belong to subgroup A1, and events A0605 and A0721 are in subgroup A2. In other words, delay times in the high-frequency components relative to the low-frequency components are different between subgroups A1 and A2 (blue frames in Fig. 5). Delay patterns for events in the same subgroup (pink and red frames in Fig. 5) do not show prominent differences between high- and low-frequency components, suggesting the delay patterns are not random but come in two types.

If the DDHL originates from the difference in the source process between events in the two subgroups, we can relate the arrival time of the low-frequency wave to the centroid time and the arrival time of the high-frequency wave to the timing of high-frequency radiation. Then the DDHL between two events belonging to different subgroups can be interpreted as the interevent difference in the time interval between the centroid time and the origin time of high-frequency radiation. For A1/A2 pairs in Fig. 5, positive slopes mean that the delay time in the high-frequency band relative to the low-frequency band for A2 is larger than that for A1, indicating that the origin time of high-frequency radiation relative to the centroid time for A1 is earlier than that for A2.

Phases calculated using F- and P-windows for all pairs are shown in Figs S6 and S7. We found that the phases calculated using the F-window (Figs 7a and d) and the P-window (Figs 7b and e) have very similar inclination angles in the high-frequency band (thus almost the same DDHL) as those using the S-window (Figs 7c and f). These facts support the idea that the observed difference in the high-frequency wave originates mainly from the difference in the source process, as discussed in Section 6.1.

Fig. 8 shows the S-window coherences for all the event pairs in group A. The very high coherences (∼1) in the frequency band lower than the corner frequencies for all the pairs indicate that the events share the same source area. We found that the A1/A1 pairs (pink lines in Figs 8a–c) and A2/A2 pair (red lines in Figs 8a–c) show relatively high coherences (∼0.6 or higher) even in the frequency bands higher than the expected corner frequencies. On the other hand, A1/A2 pairs (blue lines in Figs 8d–f) show relatively low coherences (∼0.6 or lower) in the higher frequency bands. This suggests that the rupture processes for subgroups A1 and A2 are significantly different. Similar patterns of coherences are observed at all the stations: high coherences for the A1/A1 and A2/A2 pairs and low coherences for the A1/A2 pairs in the high-frequency band.

We also found that even A1/A2 pairs have coherences higher than 0.6 in certain high-frequency bands (black horizontal lines in Figs 8d–f; HS5: ∼12–28 Hz; MY3 and SN3: ∼32–48 Hz). This indicates that similar waves exist in high frequency bands and they are prominent in these frequency bands.

Fig. 9 shows amplitude spectra (Figs 9a–c) and spectral ratios to A0505 for group A (Figs 9d–f) calculated using the S-window. The amplitude spectra were calculated as square roots of power spectra computed using eq. (7). We found that differences in the amplitude spectra between A1 events and A2 events are relatively large as expected from the results of coherences. Also, spectral ratios tend to be flat in the frequency bands where coherences are high.

5.2.2 *Groups B and C*

Figs 10 and 11, respectively show the phases and coherences calculated using the S-window for groups B and C. Phases calculated

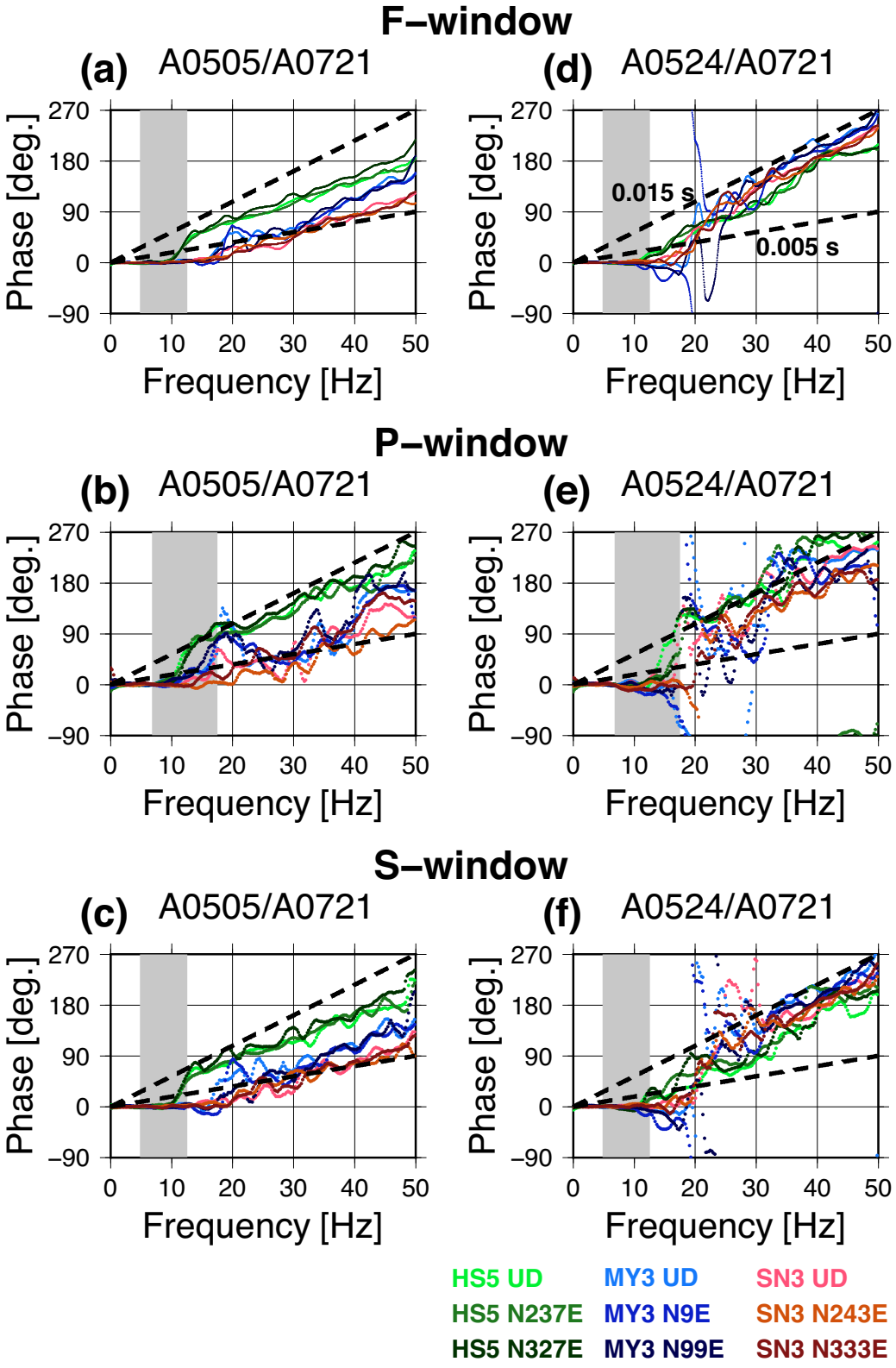

Figure 7. Phases of cross-spectra calculated using the 32.768 s F-window (top panel), the 4.096 s P-window (middle panel), and the 4.096 s S-window (bottom panel). (a–c) A0505/A0721 pair. (d–f) A0524/A0721 pair. Each trace is coloured according to the station-component set as shown at the bottom. The shaded regions indicate the range of expected corner frequencies of *S* waves (F- and S-windows) and *P* waves (P-window) for *M*3.1–3.5 events. The broken black lines represent inclination angles corresponding to 0.005 and 0.015 s time delays. Positive slopes mean that the delay time in the high-frequency band relative to low-frequency band for A2 is larger than that for A1. Note that the inclination angles (i.e. interevent delays) in the frequency bands higher than the corner frequencies are almost the same for each event pair regardless of the time windows.

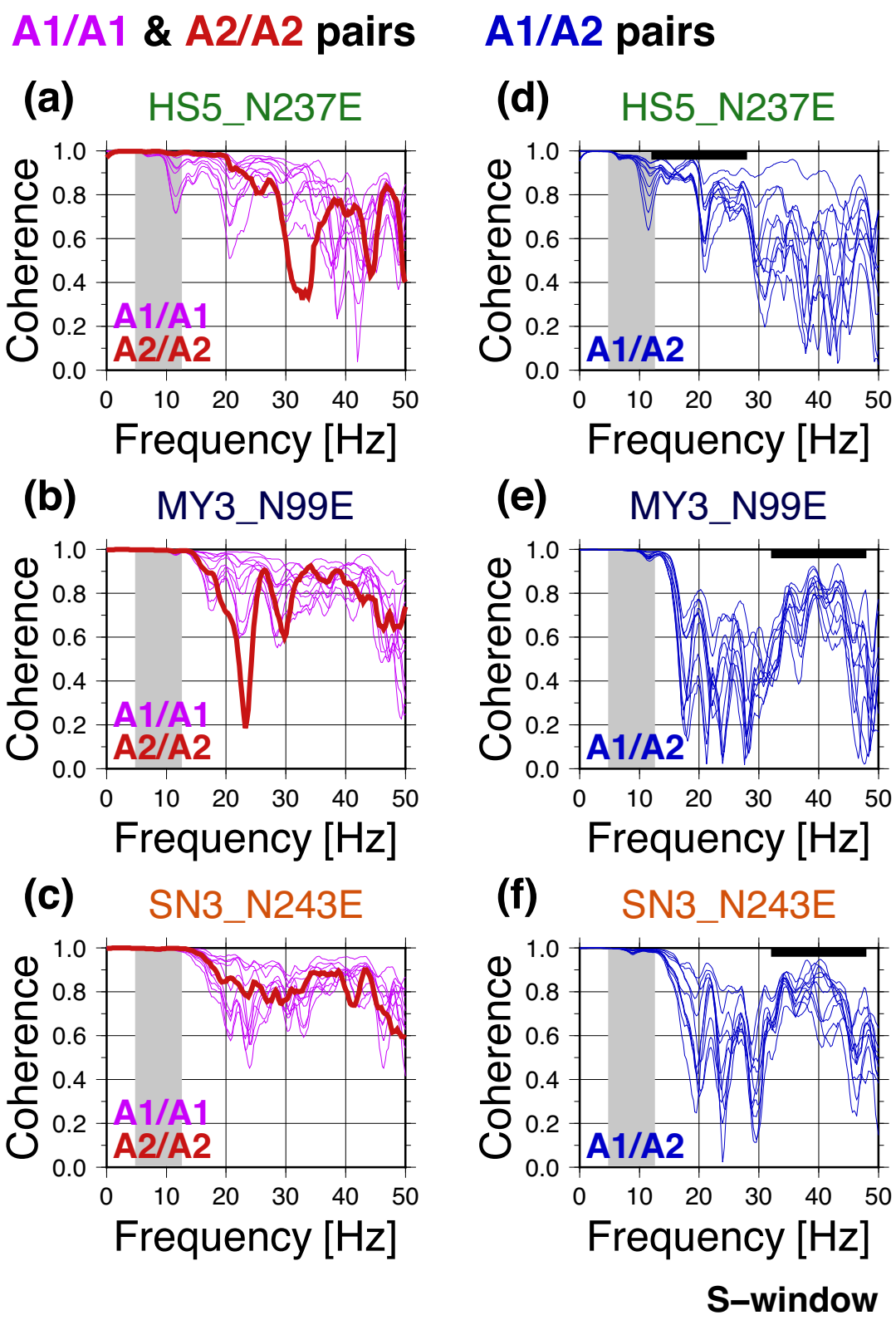

Figure 8. Coherences for all event pairs in group A calculated using the S-window for station-component sets of HS5-N237E (a, d), MY3-N99E (b, e) and SN3-N243E (c, f). Figures on the left show the results for all A1/A1 pairs (thin pink lines) and an A2/A2 pair (bold red lines), and those on the right show the results for all A1/A2 pairs (thin blue lines). The shaded regions indicate the range of their expected corner frequencies. The black horizontal bars in (d)–(f) indicate the frequency ranges showing relatively high coherences in bands higher than the corner frequencies.

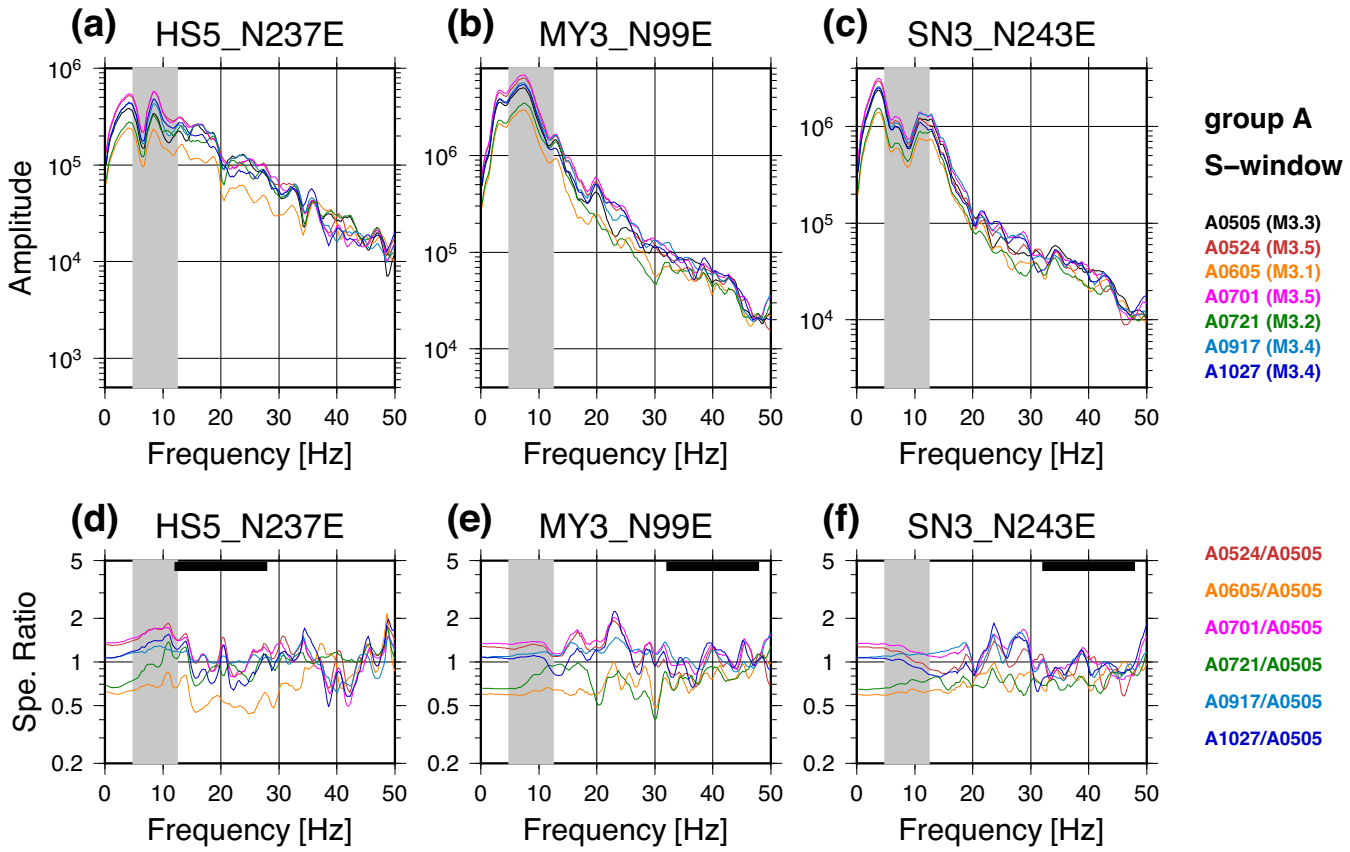

Figure 9. Amplitude spectra of events in group A calculated using the S-window for station-component sets of HS5-N237E (a, d), MY3-N99E (b, e) and SN3-N243E (c, f). (a–c) Amplitude spectra of velocity seismograms. Colours represent the events as shown in the right. (d–f) Spectral ratios relative to A0505. Different event pairs are plotted in different colours as shown in the right. The shaded regions indicate the range of their expected corner frequencies. The black horizontal bars in (d)–(f) indicate the frequency ranges showing relatively high coherences in bands higher than the corner frequencies.

using the F- and P-windows are shown in Figs S8 and S9, respectively, which show similar patterns with the S-window.

For all the event pairs in group B, the phases show no clear interevent delay in the high-frequency components (Fig. 10, top panel) and the coherences show a similar pattern (Fig. 11, left-hand panel), indicating that there are no subgroups in group B unlike the case for group A.

On the other hand, for group C, the C0529/C0804 pair shows relatively small interevent delays and higher coherences in the high-frequency band, but the C0502/C0529 and C0502/C0804 pairs show clear interevent delays and lower coherences in the high-frequency band (Fig. 10, bottom panel and Fig. 11, right-hand panel), which suggests that the rupture process for C0502 differs from the others. We also found in certain high-frequency bands, shown by black horizontal lines in Figs 11(d)–(f) (HS5: ∼8–15 Hz, MY3: ∼6–18 Hz, and SN3: ∼10–20 Hz), the coherences for the C0502/C0529 and C0502/C0804 pairs are relatively high, similar to those for the A1/A2 pairs.

As was done for the group A, we divided group C into subgroups C1 (C0502) and C2 (C0529 and C0804). The DDHLs for the C1/C2 pairs are ∼0.015–0.030 s from the inclination angles of the frequency-phase diagrams in Fig. 10. For C1/C2 pairs, the delay time in the high-frequency band relative to the low-frequency band for C1 is larger than that for C2, suggesting that the origin time of high-frequency radiation associated with C2 is earlier than that associated with C1 relative to the respective centroid times.

6 DISCUSSION

6.1 Contribution of source process differences to waveform differences

We utilized systematic differences among the high-frequency waves to define subgroups for groups A and C, though the centroid locations of events belonging to each group are very closely clustered (Fig. 3).

There are two main possible causes for the differences among the high-frequency components: (1) frequency-dependent temporal changes in the seismic velocity along the ray paths and/or changes in the site/instrument responses, (2) differences in the rupture process for two earthquakes (i.e. differences in the spatio-temporal distribution of moment release). If the differences among the high-frequency components originate from changes in velocity structures and/or site/instrument responses, the patterns of cross-spectra at different stations would not necessarily be similar because the effects of structure/site/instrument changes on waveforms would not be expected to be the same for all stations. On the other hand, if the differences originate from changes in source processes, the waveforms at all the stations would change in the same manner for all the time windows.

Based on the three facts listed below, the differences in the interevent delay between the high- and low-frequency components (DDHLs) for event pairs in subgroups A1 and A2 can be better explained by differences in the source process rather than by changes in the structures or site/instrument responses:

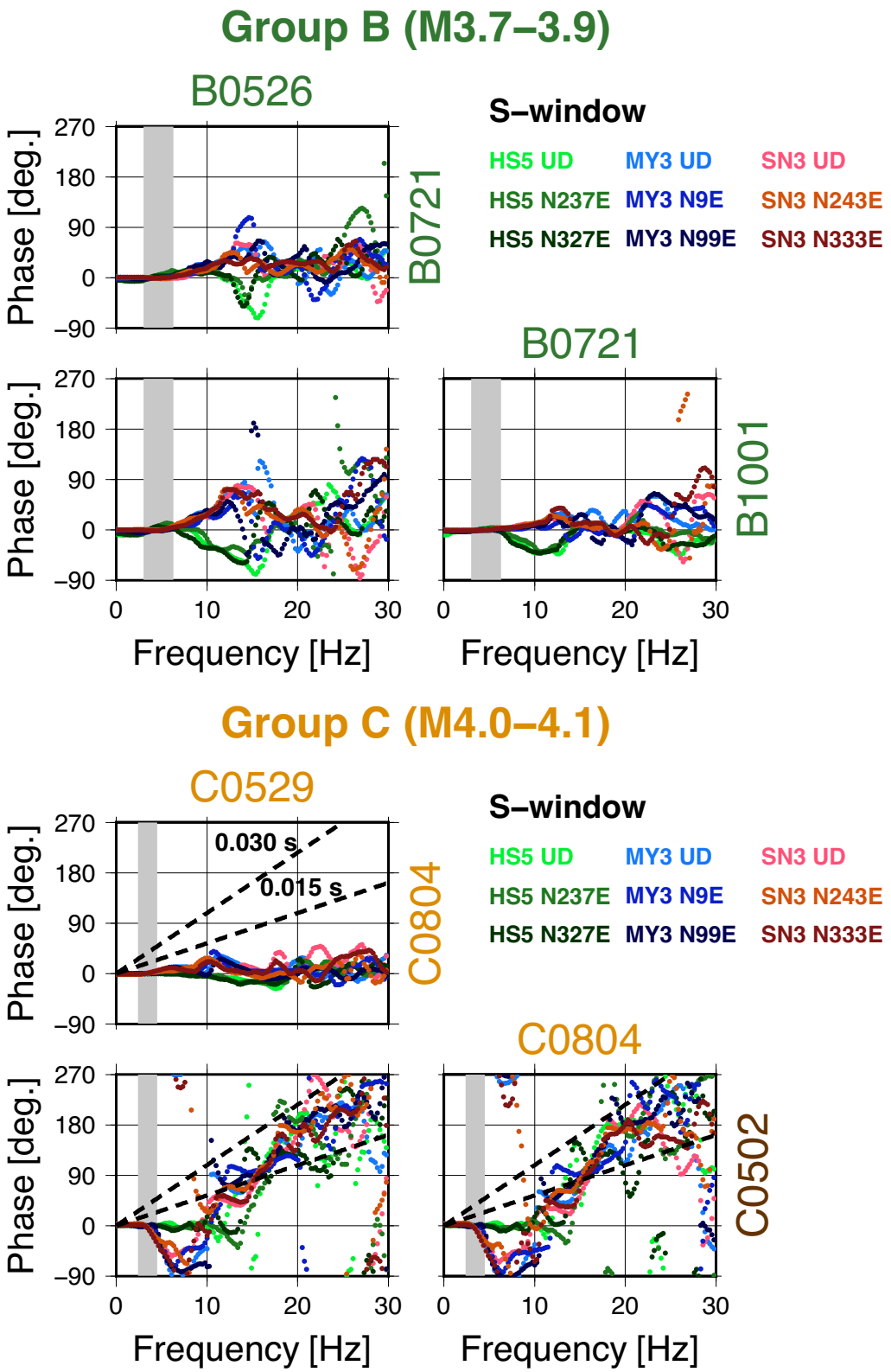

Figure 10. Phases of S-window cross-spectra for all event pairs in groups B (top panel) and C (bottom panel). Each trace is coloured according to the station-component set as shown in the upper right-hand panel. The shaded regions indicate the range of expected *S*-wave corner frequencies for *M*3.7–3.9 (top panel; group B) and *M*4.0–4.1 events (bottom panel; group C). The broken black lines in the panels for group C represent inclination angles corresponding to 0.015 and 0.030 s time delays. For C1/C2 pairs, positive slopes mean the delay time in the high-frequency band relative to low-frequency band for C1 is larger than that for C2.

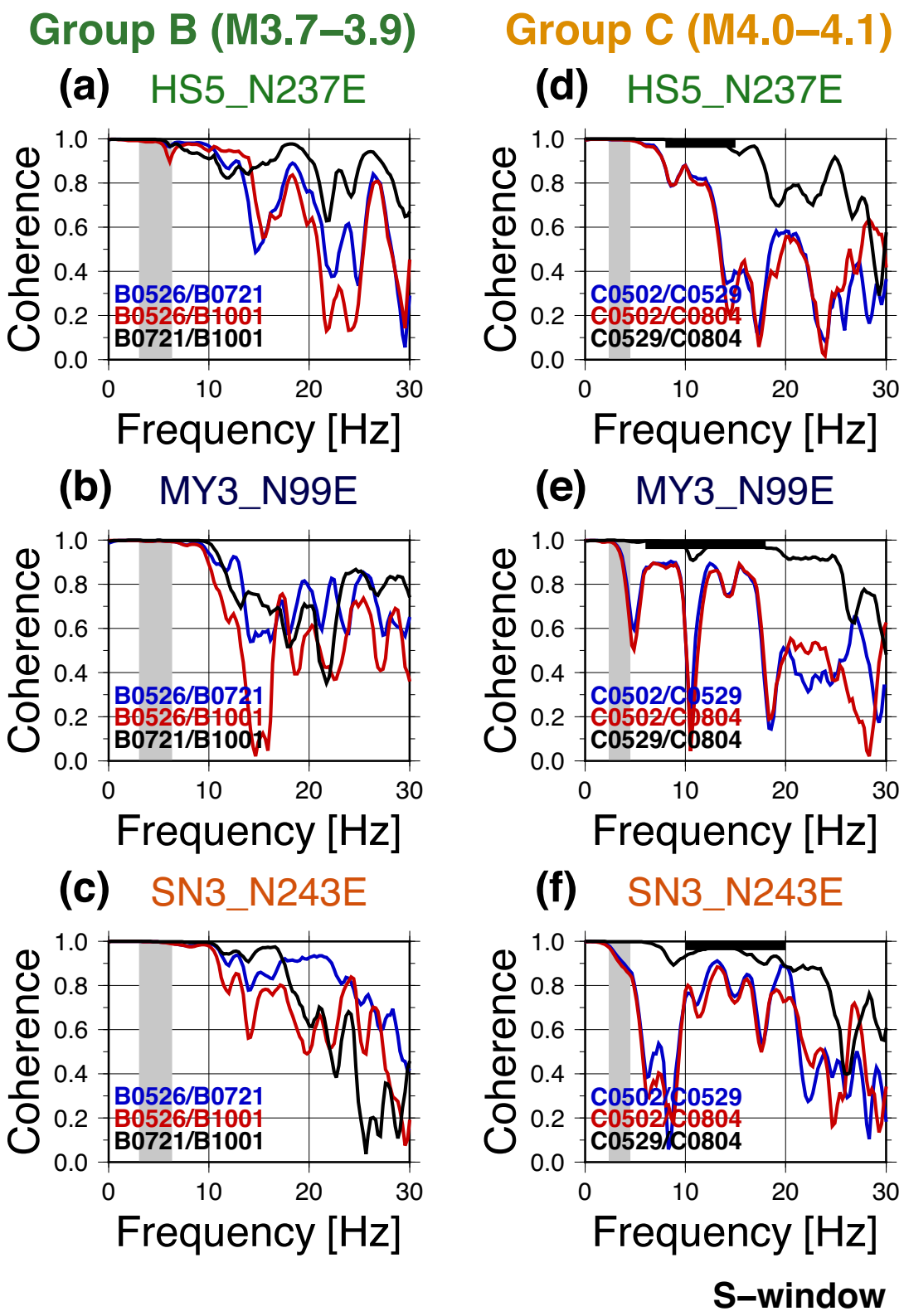

Figure 11. S-window coherences for all event pairs in groups B (left-hand panel) and C (right-hand panel) for station-component sets of HS5-N237E (a, d), MY3-N99E (b, e) and SN3-N243E (c, f). Each trace is coloured according to the event pair as shown in the lower left in each panel. The shaded regions indicate the range of expected *S*-wave corner frequencies for *M*3.7–3.9 (left-hand panel; group B) and *M*4.0–4.1 events (right-hand panel; group C). The black horizontal bars in (d)–(f) indicate the frequency ranges showing relatively high coherences in bands higher than the corner frequencies.

(1) As noted in Section 5.2, distinct DDHLs and low coherences in the high-frequency components are observed in the seismograms for all available stations and components (Figs 5 and 8). In addition, the amounts of the DDHLs do not depend on the time windows we used (Fig. 7). It is unlikely that the effects of structure/site/instrument changes on the seismograms at all the stations would be quantitatively the same for all time windows.

(2) Events in subgroups A1 and A2 occurred alternately from May to July 2011 (Fig. 2b). When trying to explain the waveform differences by structure/site/instrument changes, we have to assume that the structure/site/instrument effects that explain waveforms for events A1 and A2 alternated within a short period. Such a change is very unlikely to occur.

(3) Significant wave differences appear not at random but only in the frequency bands higher than the expected corner frequencies that correspond to the sizes of the rupture areas. Such a correspondence suggests that the differences in the waveform are related to the differences in the source process.

Thus for subgroups A1 and A2, we conclude that the source process differences are more significant than structure/site/instrument changes for the causes of the DDHL, although the latter might contribute to some extent. Waveform differences in the C1/C2 pairs (Fig. 10 bottom and Fig. 11 right) can be also explained by source process differences for the reasons (1) and (3) listed above.

6.2 High-frequency sources

For subgroups A1/A2 and C1/C2, the clear linearity of the phases (Figs 5, 7 and 10) and the existence of relatively high coherence bands (Figs 8 and 11) above the corner frequencies indicate that there are coherent waves that dominate the high-frequency components of the waveforms for all events in the groups. This suggests that there are specific sources that radiate the dominant high-frequency waves in the rupture area for the repeater and the high-frequency sources are located at almost the same place because similar high-frequency waves would not be observed if the locations of the sources vary from event to event.

The interevent delay difference between the high- and low-frequency components (DDHL) observed for time window l at station k for a pair of events i and j (Δt_{ijkl}) corresponds to the interevent difference between the arrival times of the high-frequency waves from the respective high-frequency sources (t_h^{ikl}, t_h^{jkl}) relative to the arrivals of the low-frequency waves from the respective centroid locations (t_c^{ikl}, t_c^{jkl});

$$\Delta t_{ijkl} = \left(t_h^{ikl} - t_c^{ikl}\right) - \left(t_h^{jkl} - t_c^{jkl}\right), \tag{11a}$$

$$= \left\{\left(\tau_h^i + T_h^{ikl}\right) - \left(\tau_c^i + T_c^{ikl}\right)\right\} - \left\{\left(\tau_h^j + T_h^{jkl}\right) - \left(\tau_c^j + T_c^{jkl}\right)\right\}, \tag{11b}$$

where τ_h and τ_c, respectively, represent the origin time of high-frequency radiation and the centroid time, and T_h^{kl} and T_c^{kl} represent the travel times of waves that are dominant in window l to station k from the high-frequency source and from the centroid, respectively. In this case, the waves can be not only direct waves but also later phases such as reflected waves.

When neither the high-frequency source location nor the centroid changes from event to event, travel times from the respective sources to the station remain constant for the events i and j ($T_h^{ikl} = T_h^{jkl}$, $T_c^{ikl} = T_c^{jkl}$). Then the DDHL can be expressed as;

$$\Delta t_{ijkl} = \left(\tau_h^i - \tau_c^i\right) - \left(\tau_h^j - \tau_c^j\right). \tag{11c}$$

Eq. (11c) indicates that the DDHL depends neither on the station location nor the analysis window. The observed DDHLs are almost the same for the F-, P- and S-windows at all stations for most of the event pairs (Figs 5, 7 and 10), which is consistent with the assumption. On the other hand, if the centroid and the high-frequency source vary, $(T_h^{ikl} - T_c^{ikl}) - (T_h^{jkl} - T_c^{jkl})$ would be different from phase to phase (e.g. *P* and *S*) and from station to station. Then, Δt_{ijkl} would vary from phase to phase and from station to station.

Actually, in some event pairs in group A, DDHLs for station HS5 and stations MY3 and SN3 are slightly different by up to ∼0.005 s (Figs 5 and 7). This suggests that the centroid and/or high-frequency source location vary slightly. The time lag of 0.005 s corresponds to ∼22 m assuming *S*-wave velocity of 4.4 km. The hypocentre relocation result indicates that the centroids vary to some extent (Fig. 3: within ∼50 m considering the location uncertainties), which can explain the interstation differences. In addition, the influence of the location differences on the waveform similarity in the high-frequency band is expected to be larger than that in the low-frequency band. Thus it is probable that the interevent location variance in the high-frequency sources is smaller than that in the centroid locations.

In contrast to the A1/A2 and C1/C2 pairs, the coherences in the high-frequency components are high and the DDHLs are very small among events in the same subgroup. This can mean that the differences among rupture processes are relatively small and relative timings of high-frequency radiations are almost the same for these pairs. Note that some A1/A1 pairs show nonzero DDHLs, which suggests that there are slight differences in the timing of high-frequency radiation even within subgroup A1.

Among group B, the coherences and phases in the high-frequency components do not show clear evidence for coherent high-frequency radiations (Figs 10a–c and 11a–c) but we cannot rule out the possibility that a high-frequency source exists in the rupture area for the group B events. Even when the high-frequency source does not vary from event to event, DDHLs would be zero if the timings of the high-frequency radiations relative to the centroid times do not vary and/or the high-frequency source and centroid are located at almost the same place.

6.3 A possible model to explain timing differences among high-frequency components

Our observations and explorations in the previous sections suggest that the sources of main high-frequency waves do not vary for some sequences. Based on this, we developed a conceptual model to explain the relative timing differences in the high-frequency components observed for groups A and C, which we call the 'high-frequency patch model' (Fig. 12).

In this model, there is a high-frequency patch (HFP) within the rupture area for the repeaters, which radiates coherent strong high-frequency waves during each rupture (red circle in Fig. 12a). When an earthquake occurs, the area surrounding the HFP also slips seismically together with the patch (Fig. 12a). We assume that the wave energy from the HFP exceeds the wave energy from the surrounding rupture area in the high-frequency band (Fig. 12b). In other words, the wave from the HFP dominates the high-frequency components. The overall rupture processes, including rupture initiation locations (hypocentres) and rupture directions, can vary so that the relative

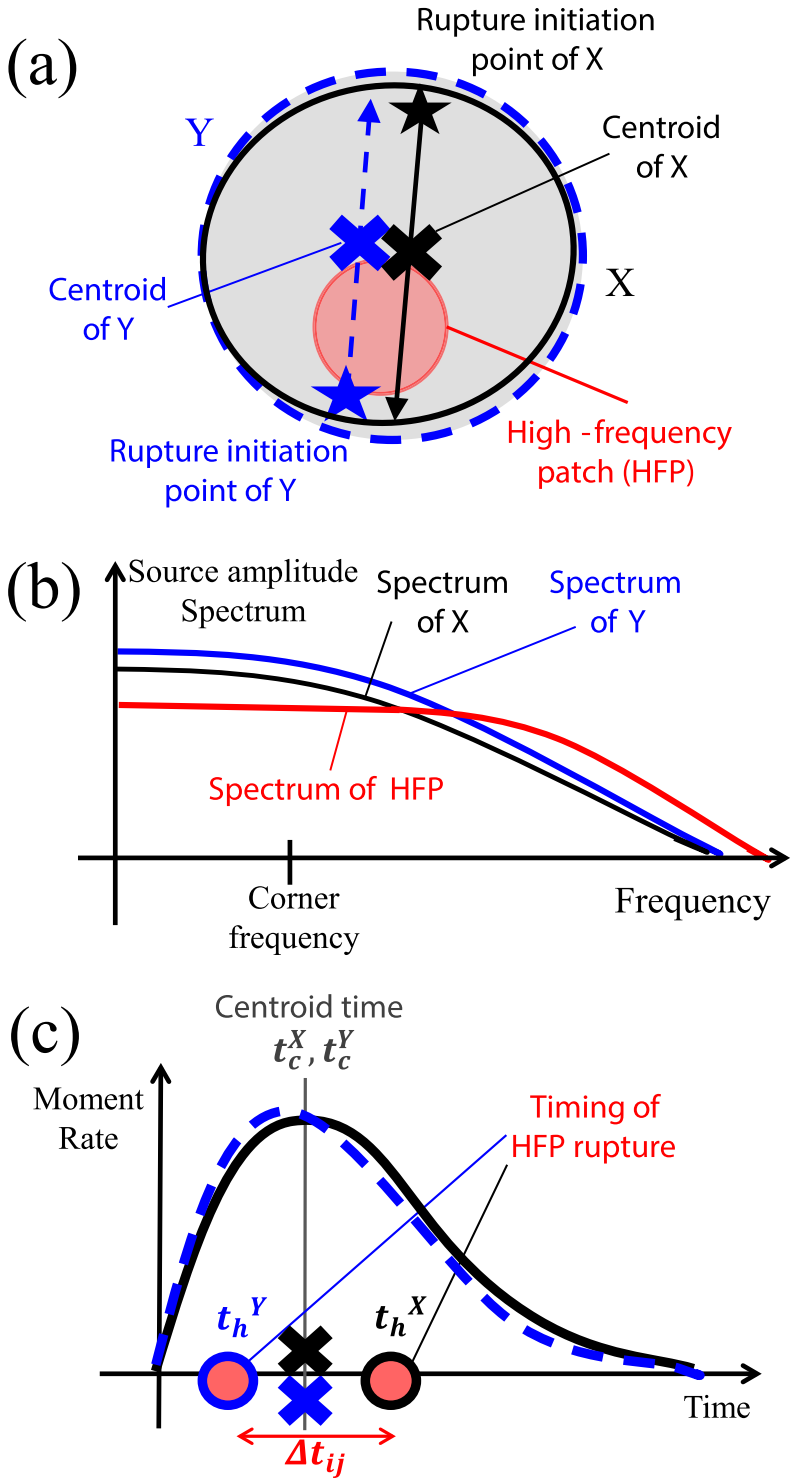

Figure 12. Schematic figures showing the conceptual 'high-frequency patch model' to explain the timing differences among the high-frequency waves. (a) Geometry of the high-frequency patch (HFP; small red circle), rupture initiation points (stars), rupture areas (large circles), and centroid locations (crosses) for events X (black) and Y (blue). The arrows represent the rupture directions for the two events. (b) Source amplitude spectra for the waves generated from the rupture of the HFP (red) and ruptures of the surrounding areas for X (black) and Y (blue). In the high-frequency band, the wave energy from the HFP is dominant. (c) Timings of HFP ruptures relative to the centroid times of entire ruptures. The black solid and blue broken lines represent the moment rate functions of X and Y, respectively. The circles and crosses show the timings of the ruptures of the high-frequency patch and centroid times of the entire ruptures, respectively. The moment rates are superimposed so that the centroid times of X and Y coincide. A red bidirectional arrow indicates the interevent differential time of the high-frequency ruptures (=DDHL).

timing of the ruptures of the HFP with respect to centroid times can differ from recurrence to recurrence (Fig. 12c). The rupture areas can also vary a little but the centroids are located at almost the same place. Then the DDHL can be expressed as the interevent difference in the time lag between the HFP rupture and the centroid time for events i and j (eq. 11c). Note that DDHL is zero when the centroid and HFP are located at the same place even if the rupture initiation points and rupture directions differ.

By way of example, we consider the simple case shown in Fig. 12. Events X and Y represent repeating earthquakes occurring at almost the same location. As shown in Fig. 12(a), X and Y have almost the same centroid locations but different rupture initiation points and rupture propagation directions. The rupture for X starts from the top and propagates toward the bottom, whereas that of Y starts from the bottom and propagates to the top. For X, the HFP ruptures after the centroid time, but the patch ruptures before the centroid time for Y (Figs 12a and c). When the source moment rate functions of X and Y are aligned so that the centroid times of the two events coincide ($t_c^X = t_c^Y$), DDHL (Δt_{ij}) corresponds to the red bidirectional arrow in Fig. 11(c), which results in the high-frequency wave differences.

Using Brune-type source models (Brune 1970), we carried out a simple simulation based on the hypothesis shown in Fig. 12. In the simulation as shown in Figs S10–S13, we successfully reproduced the characteristics of the observed phases of cross-spectra and coherences for the A1/A2 pairs shown in Figs 5, 7 and 8. We also found that the centroid times estimated from the inclinations of the phases of cross-spectra in the lowest frequency band were also affected by the rupture of the high-frequency patch (HFP), and thus the obtained DDHLs were a little shorter than the difference in the time delay from the initiation of the main rupture to the HFP rupture. This should be noted in the interpretation of the DDHLs.

The interpretation of the HFP for the pattern of high-frequency waveform is obviously of a simplification of more complex source processes in the repeating earthquake asperity. We assume that rupture initiation points and rupture directions can vary in the hypothesis shown in Fig. 12, but differences in other features in rupture processes such as rupture areas and rupture velocity can also explain the differences in relative timing between the centroid time and HFP rupture. Thus our model is not a unique model. We need to estimate detailed rupture processes using waveforms from many seismic stations to constrain the model but the station distribution is limited to the west of the repeaters and only few stations are available. Until the long-term observation data from the cabled OBS system along the Japan trench (S-net) installed by NIED have been accumulated enough to test this model, it should be considered to be provisional.

6.4 Causes of rupture process differences

One possible cause for the difference in rupture processes for repeating earthquakes is the difference in stress state within the seismic patch before the earthquake occurrences. Numerical simulations of repeating earthquakes using a laboratory derived rate- and state-dependent friction law have revealed that the stress perturbation caused by afterslip following a large earthquake near the seismic patch can change the rupture processes for the repeaters (e.g. Ariyoshi *et al*. 2007). Kato (2004) conducted numerical simulations to reveal the interaction of slips on asperities and showed that earthquakes or slow-slip events that occur near the seismic patch cause the stress concentration in the perimeter of the patch and can trigger the nucleation of seismic event.

From observation results, Shimamura *et al*. (2011) suggested that differences in nearby small earthquake activities just before the Kamaishi-oki events causes the rupture process difference between 2001 and 2008 events. Some small repeating earthquake sequences showed systematically increased seismic moments after the 2004 M6.0 Parkfield earthquake (Chen *et al*. 2010) and the 2011 Tohoku EQ (Uchida *et al*. 2015) in areas where there were large afterslips, which is an example that showed the stress perturbation on the seismic patches can cause rupture process differences.

For group A, we found that A2 events occurred within 11 days of events in group B (Fig. 2b): event A0605 occurred 10 d after B0526, and A0721 occurred 4 hr after B0721. On the other hand, the time intervals between A1 and B events are more than 20 d (Fig. 2b; Table 1). Groups A, B and C are isolated from other earthquakes and there are no events except for groups B and C close to group A (Fig. 2a). Thus there are no other events that can impart the stress change more than groups B and C can. Therefore, these observations suggest that the patch responsible for the group A events ruptures to generate A1 events when there are no perturbations from the group B events, but ruptures to cause A2 events immediately after the group B events.

Subgroups C1 and C2 also have the correlation with the timing of group B. We found that no events occurred in the place of group B before 2011 May 26 from the relocation for events before the study period (Hatakeyama, 2016). An event in subgroup C1 occurred before the first group B event and two events in C2 occurred after it. Therefore it is possible that high-frequency components for the group C events systematically changed after the emergence of the group B events.

These relationships between timings of neighbour events and differences in high-frequency components suggest that differences in the stress state in and around the source areas of repeaters cause the differences in the rupture process for repeaters. Since such relationships were observed in spite of large afterslip for the Tohoku EQ in this period, the interaction of slips on patches for neighbour small earthquakes is important for the rupture processes for repeaters as well as the stress perturbation due to large earthquakes.

For reasons other than neighbouring earthquakes, the rupture patterns might change due to stress perturbations caused by slow slip events that were not detected by the observation network and/or differences in the residual stress from the previous rupture. There might also be temporary changes in the pore pressure in the source region, which would change the strength of the seismic patch.

6.5 Implication for other studies using repeating earthquakes

The features of repeating earthquakes can be used to investigate various geophysical parameters. The ray paths of seismic waves from repeaters to given stations do not vary significantly because they recur at almost the same place. Utilizing this characteristic, we can estimate changes in the crustal structure (e.g. the velocity structure) by comparing waveform differences between repeaters occurring in the same place but at different times (e.g. Poupinet *et al*. 1984; Rubinstein *et al*. 2007; Kelly *et al*. 2013). Our results suggest that the high-frequency components of the waveforms can change due to source process differences. Thus, when estimating crustal changes from repeater waveform changes, we should use the

frequency band lower than the corner frequency to avoid the effects of source process differences.

Repeating earthquakes can also be used to monitor aseismic slip on faults because they are expected to recur at the same place to catch up to the surrounding aseismic slip (e.g. Nadeau & Johnson 1998; Nadeau & McEvilly 1999, 2004). Repeating earthquakes are often classified based on their waveform similarity (e.g. Igarashi *et al.* 2003). When using bands at higher frequencies than their corner frequencies, the similarity of the waveforms for events belonging to the same sequence can decrease even if their slip areas are colocated. Thus, when classifying repeaters by their waveform similarity, we have to use frequency bands lower than the corner frequencies.

7 CONCLUSIONS

We considered processes for variations in ruptures by investigating the differences in high-frequency wave for earthquakes in repeating sequences ($M \sim 3.1$–4.1) in the northeastern Japan subduction zone. We calculated the phases and coherences of their cross-spectra using newly obtained 1 kHz sampled seismograms from temporary observations taken immediately after the 2011 Tohoku earthquake.

We found that delay times in high-frequency bands estimated from the inclination angles of the phase spectra are different from those in low-frequency bands for particular event pairs in some repeating sequences. The phases and coherences also indicate that there are coherent high-frequency waves for all repeats in the sequences. These suggest that the main high-frequency waves are radiated from almost the same area in every rupture but the relative time lags between the timings of the main high-frequency radiations and the centroid times can vary in some cases. We developed a simple conceptual model called the 'high-frequency patch model' to explain the variation in the high-frequency radiation observed in the analyses.

It seems that high-frequency wave radiations associated with recurrent earthquakes are not random but have several patterns, probably related to the structure within the seismic patch and stress perturbations around the repeaters. The variation patterns of high-frequency radiations for small repeating earthquakes would give us clues to help evaluate rupture process variations for interplate earthquakes including large earthquakes and contribute to our ability to predict strong motions associated with them for the purpose of disaster mitigation.

ACKNOWLEDGEMENTS

The high sampling rate seismic data was obtained by the 'Group for the Aftershock Observations of the 2011 off the Pacific Coast of Tohoku Earthquake' that consists of members from Hokkaido University, Hirosaki University, Chiba University, University of Tokyo, Nagoya University, Kyoto University, Kochi University, Kyushu University, Kagoshima University, National Research Institute for Earth Sciences and Disaster Resilience (NIED), and Tohoku University. We thank Y. Ohta, N. Umino, S. Matsumoto, S. Suzuki, T. Demachi, T. Kaida and all the members of the group for their efforts to conduct the temporary seismic observations in a difficult time after the Tohoku earthquake. We also thank three anonymous reviewers and editor Prof I. Grevemeyer for their thoughtful reviews of the manuscript. We used the unified earthquake catalogue produced by the Japan Meteorological Agency (JMA) and the F-net focal mechanism catalogue provided by NIED. We used waveform data from JMA, NIED, Hokkaido University, Hirosaki University and Tohoku University for earthquake relocation. The authors thank K. Ariyoshi and all the members of the Research Center for Prediction of Earthquakes and Volcanic Eruptions, Graduate School of Science, Tohoku University, for their valuable comments. Most of the figures were prepared using the Generic Mapping Tools (GMT; Wessel & Smith 1998). This work was partly supported by Japan Society for the Promotion of Science (JSPS) Grants-in-Aid for Scientific Research (KAKENHI) Grant Number 15K06260 and the Ministry of Education, Culture, Sports, Science and Technology (MEXT) of Japan, under its Earthquake and Volcano Hazards Observation and Research Program.

REFERENCES

Ariyoshi, K., Matsuzawa, T., Hino, R. & Hasegawa, A., 2007. Triggered non-similar slip events on repeating earthquake asperities: results from 3D numerical simulations based on a friction law, *Geophys. Res. Lett.,* **34,** doi:10.1029/2006GL028323.

Brune, J.N., 1970. Tectonic stress and the spectra of seismic shear waves from earthquakes, *J. geophys. Res.,* **75**(26), 4997–5009.

Chen, K.H., Burgmann, R., Nadeau, R.M., Chen, T. & Lapusta, N., 2010. Postseismic variations in seismic moment and recurrence interval of repeating earthquakes, *Earth planet. Sci. Lett.,* **299,** 118–125.

Eshelby, J.D., 1957. The determination of the elastic field of an ellipsoidal inclusion and related problems, *Proc. R. Soc. Lond.,* **241,** 376–396.

Fremont, M. & Malone, S.D., 1987. High precision relative locations of earthquakes at Mount St. Helens, Washington, *J. geophys. Res.,* **92**(B10), 10 233–10 236.

Hanks, T.C. & Kanamori, H., 1979. A moment magnitude scale, *J. geophys. Res.,* **84,** 2348–2350.

Hatakeyama, N., 2016. Slip process variability in the interpolate seismogenic area revealed by small earthquake analyses, *Master thesis,* Tohoku University, Sendai, Japan (in Japanese).

Igarashi, T., Matsuzawa, T. & Hasegawa, A., 2003. Repeating earthquakes and interplate aseismic slip in the northeastern Japan subduction zone, *J. geophys. Res.,* **108**(B5), doi:10.1029/2002JB001920.

Iinuma, T. *et al.*, 2012. Coseismic slip distribution of the 2011 off the Pacific Coast of Tohoku Earthquake (M9.0) refined by means of seafloor geodetic data. *J. geophys. Res.,* **117,** B07409, doi:10.1029/2012JB009186.

Kamae, K., Kawabe, H. & Irikura, K., 2002. Source model for the 1978 Miyagi-Oki earthquake (M7.4) in Japan, *Prog. Abst. Seism. Soc. Japan,* **A24** (in Japanese).

Kato, N., 2004. Interaction of slip on asperities: numerical simulation of seismic cycles on a two-dimensional planar fault with nonuniform frictional property, *J. geophys. Res.,* **109,** B12306, doi:10.1029/2004JB003001.

Kelly, C.M., Rietbrock, A., Faulkner, D.R. & Nadeau, R.M., 2013. Temporal changes in attenuation associated with the 2004 M6.0 Parkfield earthquake, *J. geophys. Res.,* **118,** 630–645.

Kim, A., Dreger, D.S., Taira, T. & Nadeau, N.M., 2016. Changes in repeating earthquake slip behaviour following the 2004 Parkfield main shock from waveform empirical Green's functions finite-source inversion, *J. geophys. Res.,* **121,** 1910–1926.

Matsuzawa, T., Igarashi, T. & Hasegawa, A., 2002. Characteristic small earthquake sequence off Sanriku, northeastern Honshu, Japan, *Geophys. Res. Lett.,* **29,** doi:10.1029/2001GL014632.

Nadeau, R.M. & Johnson, L.R., 1998. Seismological studies at Parkfield VI: moment release rates and estimates of source parameters for small repeating earthquakes, *Bull. seism. Soc. Am.,* **88,** 790–814.

Nadeau, R.M. & McEvilly, T.V., 1999. Fault slip rates at depth from recurrence intervals of repeating microearthquakes, *Science,* **285,** 718–721.

Nadeau, R.M. & McEvilly, T.V., 2004. Periodic pulsing of characteristic microearthquakes on the San Andreas fault, *Science,* **303,** 220–222.

Nagai, R., Kikuchi, M. & Yamanaka, Y., 2001. Comparative study on the source processes of recurrent large earthquakes in Sanriku-oki region: the 1968 Tokachi-oki earthquake and the 1994 Sanriku-oki earthquake, *J. Seismol. Soc. Jpn.,* **54**(2), 267–280 (in Japanese).

Okada, T., Yaginuma, T., Umino, N., Kono, T., Matsuzawa, T., Kita, S. & Hasegawa, A., 2005. The 2005 M7.2 MIYAGI-OKI earthquake, NE Japan: possible rerupturing of one of asperities that caused the previous M7.4 earthquake, *Geophys. Res. Lett.,* **32,** L24302, doi:10.1029/2005GL024613.

Poupinet, G., Ellsworth, W.L. & Frechet, J., 1984. Monitoring velocity variations in the crust using earthquake doublets: an application to the Calaveras Fault, California, *J. geophys. Res.,* **89,** 5719–5731.

Rubinstein, J.L., Uchida, N. & Beroza, G.C., 2007. Seismic velocity reductions caused by the 2003 Tokachi-Oki earthquake, *J. geophys. Res.,* **112,** B05315, doi:10.1029/2006JB004440.

Sato, T. & Hirasawa, T., 1973. Body wave spectra from propagating shear cracks, *J. Phys. Earth,* **21,** 415–431.

Shimamura, K., Matsuzawa, T., Okada, T., Uchida, N., Kono, T. & Hasegawa, A., 2011. Similarities and differences in the rupture process of the $M \sim 4.8$ repeating earthquake sequence off Kamaishi, northeast Japan: comparison between the 2001 and 2008 events, *Bull. seism. Soc. Am.,* **101**(5), 2355–2368.

Sun, T. & Wang, K., 2015. Viscoelastic relaxation following subduction earthquakes and its effects on afterslip determination, *J. geophys. Res.,* **120,** doi:10.1002/2014JB011707.

Suzuki, W. & Iwata, T., 2007. Source model of the 2005 Miyagi-Oki, Japan, earthquake estimated from broadband strong motions, *Earth Planets Space,* **59,** 1155–1171.

Takiguchi, M., Asano, K. & Iwata, T., 2011. The comparison of source models of repeating subduction-zone earthquakes estimated using broadband strong motion records, *J. Seismol. Soc. Jpn.,* **63**(2), 223–242 (in Japanese).

Uchida, N. & Matsuzawa, T., 2013. Pre- and postseismic slow slip surrounding the 2011 Tohoku-oki earthquake rupture, *Earth planet. Sci. Lett.,* **374,** 81–91.

Uchida, N., Matsuzawa, T., Igarashi, T. & Hasegawa, A., 2003. Interplate quasi-static slip off Sanriku, NE Japan, estimated from repeating earthquakes, *Geophys. Res. Lett.,* **30**(15), 1801, doi:10.1029/2003GL017452.

Uchida, N., Hasegawa, A., Matsuzawa, T. & Igarashi, T., 2004. Pre- and post-seismic slow slip on the plate boundary off Sanriku, NE Japan associated with three interplate earthquakes as estimated from small repeating earthquake data, *Tectonophysics,* **385,** 1–15.

Uchida, N., Matsuzawa, T., Ellsworth, W.L., Imanishi, K., Shimamura, K. & Hasegawa, A., 2012. Source parameters of microearthquakes on an interplate asperity off Kamaishi, NE Japan over two earthquake cycles, *Geophys. J. Int.,* **189**(2), 999–1014.

Uchida, N., Shimamura, K., Matsuzawa, T. & Okada, T., 2015. Postseismic response of repeating earthquakes around the 2011 Tohoku-oki earthquake: moment increases due to the fast loading rate, *J. geophys. Res.,* **120,** doi:10.1002/2013JB010933.

Uchide, T., Shearer, P.M. & Imanishi, K., 2014. Stress drop variations among small earthquakes before the 2011 Tohoku-oki, Japan, earthquake and implications for the main shock, *J. geophys. Res.,* **119,** doi:10.1002/2014JB010943.

Umino, N. *et al.*, 2006. Revisiting the three $M \sim 7$ Miyagi-oki earthquakes in the 1930s: possible seismogenic slip on asperities that were re-ruptured during the 1978 $M = 7.4$ Miyagi-oki earthquake, *Earth Planets Space,* **58,** 1587–1592.

Waldhauser, F. & Ellsworth, W.L., 2000. A double-difference earthquake location algorithm: method and application to the Northern Hayward fault, California, *Bull. seism. Soc. Am.,* **90,** 1353–1368.

Wessel, P. & Smith, W.H.F., 1998. New, improved version of Generic Mapping Tools released, *EOS, Trans. Am. geophys. Un.,* **79,** 579.

Wu, C., Koketsu, K. & Miyake, H., 2008. Source processes of the 1978 and 2005 Miyagi-oki, Japan, earthquakes: repeated rupture of asperities over successive large earthquakes, *J. geophys. Res.,* **113,** B08316, doi:10.1029/2007JB005189.

Yamanaka, Y. & Kikuchi, M., 2004. Asperity map along the subduction zone in northeastern Japan inferred from regional seismic data, *J. geophys. Res.,* **109,** B07307, doi:10.1029/2003JB002683.

SUPPORTING INFORMATION

Additional Supporting Information may be found in the online version of this paper:

Figure S1. Examples of raw waveforms for events in groups A–C for the vertical (UD) component at station HS5. See the caption of Fig. 4 for further details.

Figure S2. Examples of raw waveforms for events in groups A–C for the vertical (UD) component at station SN3. See the caption of Fig. 4 for further details.

Figure S3. Signal and noise spectra for events in group A calculated using the P-window and window before the *P*-wave onsets, respectively. Spectra for all the station-component pairs are shown. Signal spectra for different events are drawn by different colours as shown in lower right but noise spectra for all events are shown by the same grey colour. The window for the noise spectra is the same length as the signal (4.096 s) that starts from 4.596 s before the *P*-wave onset.

Figure S4. Signal and noise spectra for events in group B. See the caption of Fig. S3 for further details.

Figure S5. Signal and noise spectra for events in group C. See the caption of Fig. S3 for further details.

Figure S6. Phases of F-window cross-spectra for all event pairs in group A. See the caption of Fig. 5 for further details.

Figure S7. Phases of P-window cross-spectra for all event pairs in group A. See the caption of Fig. 5 for further details. The shaded regions indicate the range of expected *P*-wave corner frequencies for *M*3.1–3.5 events.

Figure S8. Phases of F-window cross-spectra for groups B and C. See the caption of Fig. 10 for further details.

Figure S9. Phases of P-window cross-spectra for groups B and C. See the caption of Fig. 10 for further details.

Figure S10. Source time functions (left-hand panel) and spectra (right-hand panel) for the main and sub events assumed in the simulation. Top panel: main (low-frequency) event (LFE). Middle panel: high-frequency subevent #1 (HFE1). Bottom panel: high-frequency subevent #2 (HF2). Vertical scales are arbitrary. We use Brune-type source time functions, and rupture initiation times for HFE1 and HFE2, respectively start 0.01 s after and 0.04 s after the rupture initiation of LFE. Corner frequencies for LFE and HFEs are 10 and 25 Hz, respectively.

Figure S11. Synthesized source time functions (left-hand panel) and their source spectra (right-hand panel). Top panel: source function composed of LFE and HFE1 simulating A1-type events. Bottom panel: source function composed of LFE and HFE2 simulating A2-type events.

Figure S12. Synthesized *S* wavelets (left-hand panel) and their spectra (right-hand panel). Window length is 4.096 s and the sampling frequency is 1 kHz. Green functions are simulated using a series of random pulses. Each *S* wavelet is calculated by convolving the source time function with the Green function, attenuating the waveform taking the Qs value into account, converting it into velocity seismograms, and convolving it with the response of a 1 Hz seismometer with a damping constant of 0.7. The assumed Qs value is 800 (Matsuzawa *et al*. 2002) and *S*-wave travel time is 20 s which is an average of the travel times for MY3 and SN3. Top panel: synthesized waveform and spectrum simulated for A1-type event using LFE and HFE1. Bottom panel: synthesized

waveform and spectrum simulated for A2-type event using LFE and HFE2.

Figure S13. Phases and coherences calculated from the cross-spectrum of the two synthesized waveforms. Top panel: phases of the cross-spectrum calculated directly from the two waveforms shown in Fig. S12. Vertical scales are shown in radian divided by π. Middle panel: phases calculated after re-aligning the two waveforms so that the calculated phases in the 2–8 Hz range become zero. Bottom panel: coherences. Note that the DDHL estimated from the simulation is ∼0.02 s while the difference between the two HFE rupture initiation times with respect to the LFE rupture initiation time is 0.03 s.
(http://gji.oxfordjournals.org/lookup/suppl/doi:10.1093/gji/ggw313/-/DC1).

Please note: Oxford University Press is not responsible for the content or functionality of any supporting materials supplied by the authors. Any queries (other than missing material) should be directed to the corresponding author for the paper.